# Experimental and numerical characterization of the airflow in the wake of a heavy truck

A Pérard-Lecomte, M Djeddou, G Fokoua, Amine MEHEL, A Tanière

A Pérard-Lecomte, M Djeddou, G Fokoua, Amine MEHEL, A Tanière. Experimental and numerical characterization of the airflow in the wake of a heavy truck. Physics of Fluids, 2023, 35, ⟨10.1063/5.0150404⟩. ⟨hal-04339193⟩

Physics of Fluids

AIP Publishing

RESEARCH ARTICLE | JUNE 02 2023

# Experimental and numerical characterization of the airflow in the wake of a heavy truck ✓

A. Pérard-Lecomte ✉ ; M. Djeddou ; G. Fokoua; A. Mehel ; A. Tanière

*Physics of Fluids* 35, 065104 (2023)
https://doi.org/10.1063/5.0150404

Physics of Fluids ARTICLE pubs.aip.org/aip/pof

# Experimental and numerical characterization of the airflow in the wake of a heavy truck

Cite as: Phys. Fluids **35**, 065104 (2023); doi: 10.1063/5.0150404
Submitted: 14 March 2023 · Accepted: 15 May 2023 ·
Published Online: 2 June 2023

A. Pérard-Lecomte,[1,2,a)] M. Djeddou,[1,2,3] G. Fokoua,[2] A. Mehel,[2] and A. Tanière[1]

AFFILIATIONS

[1]Universite Lorraine, CNRS, LEMTA, F-54000 Nancy, France
[2]ESTACA, 78180 Montigny-le-Bretonneux, France
[3]ARIAMIS Engineering, 92000 Nanterre, France

[a)]Author to whom correspondence should be addressed: aude.perard-lecomte@univ-lorraine.fr

## ABSTRACT

The wake flow of a heavy truck model is investigated at $Re = 8.5 \times 10^4$ using particle image velocimetry measurements combined with computational fluids dynamics-simulations. Experimental measurements are carried out on a 1:28-scale model, focusing exclusively on the central longitudinal plane, in the rear of the truck model. Numerical simulations are performed based on the URANS (unsteady Reynolds averaged Navier–Stokes) approach using two statistical turbulence models, i.e., the shear stress transport $k$–$\omega$ and the baseline Reynolds stress (BSL-RSM) models. A comparison between the numerical and experimental results of the mean velocity profiles in the wake of the heavy truck is found to be relatively consistent. The BSL-RSM model, however, gives a better prediction of experiments, with a deviation of 6% in the near wake, against 13% for the SST $k$–$\omega$. Both URANS models undervalue the streamwise and spanwise turbulence intensity components with a deviation around 24%, compared with the experimental results. The characteristic feature of the wake flow topology is the formation of a recirculation bubble resulting from the shear layers separated from the truck surfaces. Different identification methods, including visualization of closed streamlines, vorticity magnitude, and the $Q$-invariant criterion, are considered and highlight the existence of two particular vortex regions in the mean flow: a vortex-shedding area in the upper recirculation region and a back-truck attached vortical structure. It is found that the $Q$ criterion-based technique is a relevant indicator of the vortex cores regions.

## I. INTRODUCTION

Air pollution associated with road traffic represents a significant health issue. Different pollutants are encountered, including carbon monoxide (CO), nitrogen oxides ($NO_x$), sulfur dioxide ($SO_2$), hydrocarbons (HC), and particulate matter (PM) such as fine and ultrafine particles. These latter are particularly known to increase the risk of developing cardiovascular and respiratory diseases, and lung cancer, as they can penetrate deeply into the respiratory system reaching the blood and cells, for the finest ones.[1,2] The exhaust of diesel vehicles, composed mainly of particles, has been classified as carcinogenic by the International Agency for Research on Cancer.[3] In addition, non-traffic emissions, related to brake and tire abrasion, are also identified as major contributors of fine and ultrafine particles.[4,5] This type of pollution is a major problem directly affecting the air quality of pedestrians and commuters inside adjacent vehicles cabins through infiltration processes. Infiltration inside the vehicle would be even more significant when the following vehicle is a bluff-type body, such as vans, buses, and trucks.[6] This problem has, therefore, aroused the interest of environmental and health agencies, and many efforts, initiatives, and strategies have been initiated to reduce pollution from road transport and thus to improve urban air quality.

Nevertheless, the search for new optimal solutions remains a big challenge. Within this context, it seems important to characterize road traffic pollution by considering the emissions of different types of vehicles and more specifically to analyze the dispersion dynamics of particles from their release sources to their dilution in the atmosphere.

The physical mechanisms governing the dispersion of pollutants in the atmosphere are well documented. While gaseous pollutants dynamics exhibit similarities with fluid particles, i.e., passive scalars, when chemical reactions are ignored, the dispersion of particulate pollutants is quite complex. Indeed, the dynamics of inertial particles is strongly influenced by the topology of the turbulent flow, in particular by complex interactions with turbulent eddy structures.[7] This gives rise to particular behaviors, such as the well-known accumulation and clustering of particles in some preferential regions of the flow.[8–11] Such particular dynamics can be illustrated, for example, by the tendency of small inertial particles to drift out of a vortex core and concentrate in a region of a higher strain rate.[12] It has also been reported that large-scale, energetic, and anisotropic coherent structures play a key role in transport processes.[13]

Faced with this challenge, we have been interested in the air pollution resulting from road traffic of heavy trucks, specifically the influence of different parameters on the dispersion of pollutants, such as the position of the tailpipe, the emission rate, and the volume of the extent of the wake region. The objective is then to investigate the turbulent flow characteristics in order to understand more precisely the effects and the influence of the flow around a heavy truck on the spatial distribution and dispersion of particles (fine and ultrafine). This investigation could thus provide a good starting point to identify appropriate control solutions to better understand the dispersion process in order to limit or reduce the exposure of commuters to fine and ultrafine particles. This could be, for example, an optimal placement of the exhaust pipe, a source capture system made of absorbent materials, and placed at appropriate locations on vehicles…

The flow in the wake of simplified light vehicles has been extensively studied and documented by considering the well-known Ahmed body.[14–16] Similar to this simple-track car model, a simplified version corresponding to heavy vehicles was developed and referred to as ground transportation system (GTS) [Fig. 1(a)]. It consists of a single block with the dimensions of a tractor–trailer, and without any interspace or wheels. The front part of the model presents rounded edges to fit the general shape of cab-over engines, like European heavy trucks. The GTS model is characterized by an aspect ratio of height to width of approximately 1.4. This model has been studied for a wide range of Reynolds numbers, up to $2 \times 10^6$, by means of experimental techniques, using particle image velocimetry (PIV),[17–19] and numerical simulations, using large eddy simulation (LES),[20,21] improved delayed detached eddy simulation (IDDES),[22,23] RANS,[24] and partially averaged Navier–Stokes (PANS).[25]

As for Ahmed's body, the flow around the GTS geometry is very complex and highly unsteady. The flow separates from the body at the edges, creating a region of low pressure behind the body, which can be observed as a wake and is characterized by high turbulence and recirculating flow. The wake flow exhibits interesting dynamics features that can be ranged using the Strouhal number (*St*), which is a dimensionless parameter that relates the frequency of the vortex detachment to the flow velocity and to a characteristic length scale. Indeed, the bistable motion is defined by the coexistence of two asymmetric up/down vortex structures and characterized by low-frequency dynamics ($St \sim 10^{-3}$).[28,29] On the upper wall edge, the flow separates in a vortex-shedding-like motion characterized by a high frequency $St \sim 0.19$ and interacts with the recirculation bubble resulting in periodical expansion and shrinking of the whole recirculation region in a so-called pumping motion. This pumping phenomenon is a low-frequency dynamics motion that is accompanied by a vortex ejection along the wake flow at a frequency of about $St \sim 0.08$.[13,18,30–32]

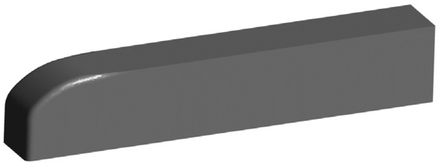

(a)

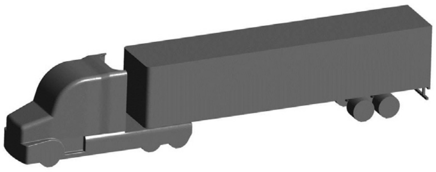

(b)

**FIG. 1.** Simplified geometries of tractor–trailer reported in the literature: (a) GTS,[26] (b) GCM.[27]

The bi-stable wake flow displays two distinct "stable" states, into which the flow can settle, each characterized by a different vortex pattern. A first state depicted in Fig. 2 was widely observed, by Refs. 17–19, 22, 23, and 25. In this case, the recirculation region contains a main triangular vortex against the truck's back wall (blue lines in Fig. 2) and a second vortex, smaller in size and of elliptical shape, located at the top of the recirculation bubble (red lines in Fig. 2). A second state was observed,[20,21,24] which is almost symmetrical to the first state, about the longitudinal central axis of the truck. Although the wake flow topology of the GTS model is well described for a given configuration, there are, however, several parameters that influence this flow in the wake.

The topology of the wake flow was found to be strongly influenced by the aspect and clearance ratios, respectively, defined as the ratio of the truck's height/width and ground clearance/height.[18,23] While the recirculation region always contains two main counter-rotating vortices for an aspect ratio in a range of 1.0–2.0, the shape and position of these two vortices vary, leading to a more or less symmetric wake flow.[23] The wake flow topology remains unchanged for a clearance ratio between 0.14 and 1.1, as there is sufficient space for the flow to remain undisturbed between the GTS model and the ground. When the clearance ratio is progressively reduced to 0.03, three new flow topologies are observed, in which the counter-rotating vortices take different sizes, shapes, and locations.[18] The velocity under the truck was also found to have a significant influence on the topology of the wake flow.[19] However, Castelain *et al.*[19] have mentioned that heavy trucks' underbody velocities are actually less than half of the free-flow velocity, due to the presence of wheels, axles, and other underbody components. Consequently, simplified models, such as the GTS model, present some limitations, as they are considered with unrealistic clearance ratios and sub-body velocities, leading to non-representative wake flow topologies. Therefore, the GTS model appears to be too simplified to be considered in the study of particulate

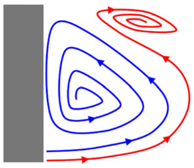

**FIG. 2.** Schematic of streamlines in the wake of the GTS, observed by Refs. 17–19, 22, 23, and 25, in the vertical longitudinal midplane of the model. The gray area represents the back of the GTS. The wake flow consists of a large triangular vortex attached to the truck's rear surface (blue streamline) and a small elliptical vortex located higher in the recirculation region (red streamline).

dispersion from heavy-duty truck emissions. It is, thus, necessary to investigate more realistic and detailed tractor–trailer models.

A realist simplified model of heavy trucks, known as the general conventional model (GCM) [Fig. 1(b)], has also been extensively investigated in the published literature. Compared to the GTS model, the GCM includes a tractor part and a trailer part separated by a space in between and other components, such as wheels and axles in the sub-trailer. The GCM has been considered in a number of aerodynamic studies,[27,33–36] where the focus was mostly on drag-reduction solutions for fuel economy purposes and a few on the flow topology around the heavy truck model.[35] Additional realistic tractor–trailer geometries, slightly different from the GCM, were considered.[13,37–42] The recirculation regions obtained for these realistic heavy ground vehicle variants differ slightly from the airflow observed in the GTS model. However, the main vortex attached to the trailer back (blue vortex in Fig. 2) is present behind both simplified and realistic geometries. Despite the available studies on the characterization of the wake flow of simplified heavy trucks, the flow topology behind a realistic tractor–trailer such as the GCM geometry remains poorly documented.

Therefore, in this paper, we are interested in understanding and modeling the wake flow of a tractor–trailer with a particular focus on the identification of vortex structures considering the significant influence they play in the dispersion of particulate pollutants. The objectives of the present study are thus

- to characterize the flow and coherent structures developing in the wake of a simplified heavy truck (GCM),
- to examine the relevance of some vortex structure identification methods applied to the wake flow, and
- to evaluate the performance of two URANS turbulence models in simulating a highly turbulent three-dimensional flow.

In Sec. II, the experimental and numerical methodologies, consisting of PIV and RANS techniques, are briefly presented, and in Sec. III, the flow topology is discussed, followed by a comparison between measurements and computational fluids dynamics (CFD)-simulations results of the heavy truck wake flow.

## II. METHODOLOGY

### A. Experimental methodology

#### 1. Test facility

In this study, a simplified, reduced-scale (1:28) version of a GCM model [Figs. 1(b) and 3], previously reported in Refs. 27 and 33–36, was used. This model is representative of typical North American semi-trailers with a projected nose-shaped style, with a conventional-type cab mounted behind the engine. Its length $L$ and width $W$, are, respectively, 699 and 93 mm. The characteristic length of the heavy truck is considered as the height of the trailer, which is equal to 103 mm (Fig. 3) $H/W$ is therefore 1.11. The ground clearance $C$ of 42 mm (Fig. 3), determined by the wheels and axles dimensions, leads to a clearance ratio $C/H$ of 0.41. In the results presented further, the origin of the reference frame has been taken in the middle of the trailer rear (Fig. 3).

Measurements were performed in an open-circuit wind tunnel shown in Fig. 3 fitted with a test section of 600 mm side square and 1.50 m long. A honeycomb structure was placed upstream of the test section's entry (Fig. 3) to damp large-scale turbulence. Figure 4 gives the turbulence intensity measured at the wind tunnel inlet, which was found to be less than 2%. A stationary raised floor with a rounded leading edge allows having a zero-thickness boundary layer at the entrance of the test section. The boundary layer thickness reaches 19 mm at the end of the raised floor. The tractor–trailer model was placed 130 mm downstream of its leading edge on this floor (Fig. 3). In this configuration, the blockage ratio of the model to the test section frontal surfaces was below 5 %, as advised by Gross and Sekscienski.[43]

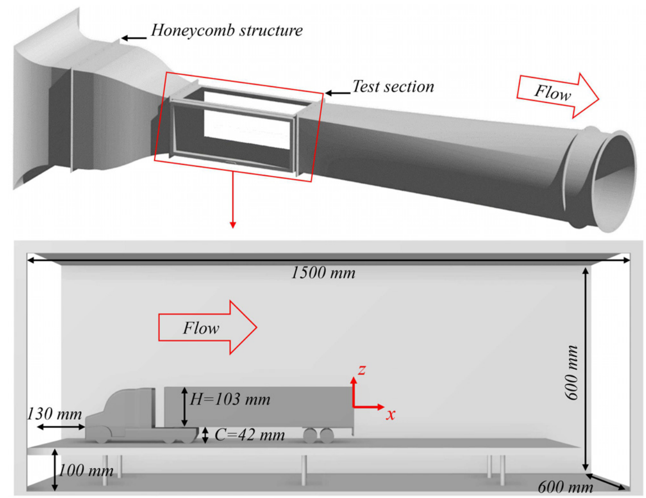

**FIG. 3.** Wind tunnel and 1:28-scale tractor–trailer model placed in the test section, with noticeable dimensions.

The following results are presented for an upstream velocity $U_0$ of $12\,\mathrm{m\,s^{-1}}$, corresponding to a Reynolds number $Re = U_0 H/\nu = 8.5 \times 10^4$ based on the trailer's height, where $\nu$ is the air kinematic viscosity.

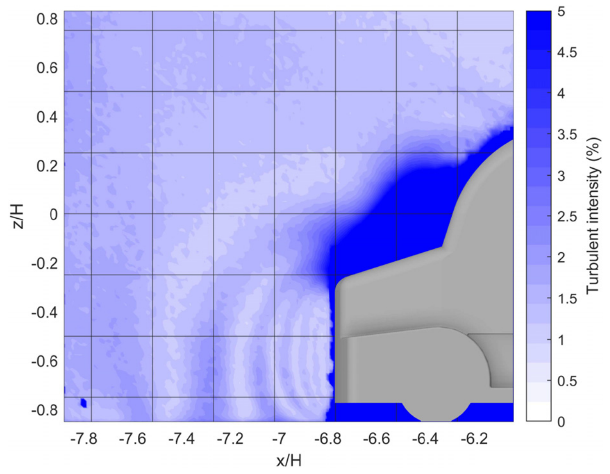

**FIG. 4.** Turbulent intensity ($u'/U_0$) upstream of the truck model measured in the wind tunnel. The gray area represents the front of the tractor. Turbulent intensity is lower than 2% away from the walls.

### 2. Measurement technique

Velocity measurements in the longitudinal vertical central *xz*-plane of the heavy truck model were acquired using a 2D2C particle image velocimetry (PIV). The focus was directed exclusively to the back of the vehicle to study the downstream flow at $Re = 8.5 \times 10^4$. A single case has, therefore, been investigated in the present study.

Figure 5 depicts the main PIV devices and their relative position to the truck. The fog generator *S195G* from *SAFEX*, associated with a mix of water and diethylene glycol, was used to seed the test section. Particles were illuminated in a vertical laser plane, generated by a double-pulsed *LASER Nd-YAG* from *DANTEC*, located above the test section (Fig. 5). It is characterized by a wavelength of 532 nm and pulse energy of 135 mJ. The thickness of the LASER sheet was around 2 mm. Pictures of the enlightened moving particles were taken with a 4 Mpx camera *FlowSenseEO 4M-32* (Fig. 5), which is fitted with a CCD sensor resolution of $2072 \times 2072\,\text{pixels}^2$. *DynamicStudio* software from *DANTEC* was used for the image cross correlation processing to obtain $2D-(xz)$ velocity vector maps.

The magnification factor in this configuration was around 12.7. The default size of the interrogation area was $32 \times 32\,\text{pixels}^2$, leading to a final spatial resolution of 1.51 mm, corresponding to $0.015\,H$. The time step between two pulses was set to $55\,\mu$s for an upstream velocity of $12\,\text{m s}^{-1}$. Samples of image pairs were acquired with a frequency of 15 Hz. The results of mean quantities were then obtained by time-averaging a total of $N = 1000$ pairs of images, corresponding to a measurement duration of 66.7 s.

Following Sciacchitano and Wieneke,[44] uncertainties on the mean velocity $\mathcal{U}_{\bar{u}}$ and of Reynolds stresses $\mathcal{U}_{\overline{u'u'}}$, $\mathcal{U}_{\overline{w'w'}}$ can be evaluated as follows:

$$\mathcal{U}_{\bar{u}} = \frac{\sigma_u}{\sqrt{N}} = \frac{\overline{u'}}{\sqrt{N}}, \tag{1}$$

$$\mathcal{U}_{\overline{u'u'}} = \sigma_u^2\sqrt{\frac{2}{N-1}} = \overline{u'}^2\sqrt{\frac{2}{N-1}}, \tag{2}$$

$$\mathcal{U}_{\overline{w'w'}} = \sigma_w^2\sqrt{\frac{2}{N-1}} = \overline{w'}^2\sqrt{\frac{2}{N-1}}, \tag{3}$$

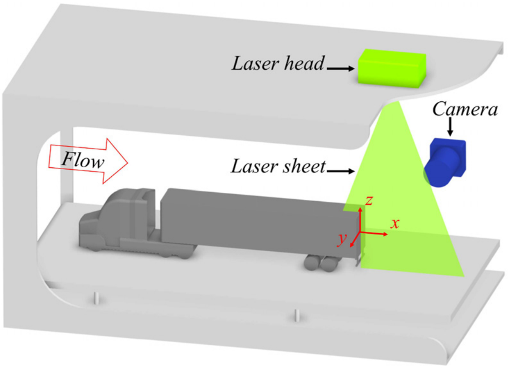

**FIG. 5.** Truck model in the wind tunnel test section and PIV-devices, focused on the wake of the heavy truck.

where $\sigma_u$ and $\sigma_w$ are the standard deviations of velocity components $u$ and $w$. $\sigma_u$ and $\sigma_w$ correspond thus to time-averaged fluctuating $x-$ and $z-$ velocity components, noted, respectively, $\overline{u'}$ and $\overline{w'}$. For a complete PIV map acquired in the wake of the truck, the spatially averaged standard deviations are $\sigma_u = 1.44\,\text{m s}^{-1}$ and $\sigma_w = 1.34\,\text{m s}^{-1}$. The estimated uncertainty values are summarized in Table I. For the three quantities, the error percentage does not exceed 1 %, vindicating the reliability of experimental measurements.

## B. Numerical methodology

### 1. Modeling approach

Simulations were conducted using the incompressible unsteady Reynolds-averaged Navier–Stokes (URANS) approach. It is based on the Reynolds decomposition, in which any flow variable is decomposed into its mean and fluctuating quantities. This allows for deriving the averaged equations that govern the mean flow behavior. The averaged momentum equation and the velocity field divergence-free condition which governs the mean flow dynamics are defined as follows:

$$\frac{\partial \bar{u}_i}{\partial t} + \bar{u}_j\frac{\partial \bar{u}_i}{\partial x_j} = -\frac{1}{\rho}\frac{\partial \bar{p}}{\partial x_i} + \frac{\mu}{\rho}\frac{\partial^2 \bar{u}_i}{\partial x_j^2} - \frac{\partial}{\partial x_j}\left(\overline{u_i'u_j'}\right), \tag{4}$$

$$\frac{\partial \bar{u}_i}{\partial x_i} = 0, \tag{5}$$

where $\rho$ is the density, $\bar{u}_i$ represents the mean velocity components, and $u_i'$ represents the fluctuating velocity components. $\bar{p}$ is the mean pressure and $\mu$ is the dynamic viscosity.

In order to close the set of the URANS equations, the statistical correlations of the fluctuating velocity components $\overline{u_i'u_j'}$, known as the Reynolds stress tensor, must be determined. This consists in modeling the effect of turbulence on the mean flow behavior. In the present study, two turbulence models based on two different closure approaches are investigated. A first-moment closure-based model, namely the shear-stress transport (SST) $k$–$\omega$ model ($k$ is the turbulent kinetic energy and $\omega$ is the specific dissipation rate), and a second-moment closure-based model, i.e., the baseline Reynolds stress model (BSL-RSM), are both examined. These two models have demonstrated some capabilities in producing some complex flows such as airflow inside car cabins of the velocity and turbulence quantities. They also appear to return realizable solutions of the Reynolds stress components and allow capturing the anisotropic structure of the turbulence.[45]

Note that two other models of closures have been considered, a second-moment closure-based model namely the $\omega$-Reynolds stress model, and also an algebraic Reynolds stress model namely the explicit algebraic Reynolds stress model (EARSM). However, in the following, we will not present them for the sake of clarity and because the results obtained are not much different, especially compared to the BSL-RSM model.

**TABLE I.** Spatially averaged uncertainty on time-averaged quantities, for $N = 1000$.

| Quantity $Q$ | Uncertainty $U_Q$ | Error percentage |
|---|---|---|
| $u$ | 0.045 | 0.37% |
| $\overline{u'u'}$ | 0.092 | 0.77% |
| $\overline{w'w'}$ | 0.080 | 0.67% |

In the first-moment closure approach, the Reynolds stress components are linearly related to the mean velocity gradients following the Boussinesq eddy-viscosity hypothesis:

$$\overline{u_i'u_j'} = \frac{2}{3}k\delta_{ij} - 2\frac{\mu_t}{\rho}S_{ij}, \tag{6}$$

where $S_{ij} = \frac{1}{2}(\partial\bar{u}_i/\partial x_j + \partial\bar{u}_j/\partial x_i)$ is the mean strain rate tensor, and $\delta_{ij}$ is the Kronecker delta. Thus, the problem of modeling the Reynolds tensor is reduced to determining the turbulent viscosity coefficient $\mu_t$ as an isotropic scalar quantity. Models based on the eddy-viscosity hypothesis are widely used in industrial applications, particularly the two-equation models. The most popular are the $k$–$\varepsilon$ and the $k$–$\omega$ models, and their variants [standard $k$–$\varepsilon$,[46] renormalization group (RNG) $k$–$\varepsilon$,[47] Realizable $k$–$\varepsilon$,[48] standard $k$–$\omega$,[49] shear-stress transport (SST) $k$–$\omega$,[50]…].

In the $k$–$\omega$ SST model, turbulent viscosity is obtained by solving two additional transport of the turbulent kinetic energy $k$, and the specific dissipation rate $\omega$, referred to as the characteristic frequency for the large eddies, $\omega \equiv \varepsilon/k$, with $\varepsilon$, the dissipation rate. This model was developed by blending between the Wilcox standard $k$–$\omega$ model in the near wall region with the standard $k$–$\varepsilon$ formulation in the outer part of the boundary layer.[50] In this case, the turbulent viscosity is expressed as follows:

$$\mu_t = \frac{\rho a_1 k}{\max[a_1\omega, SF_2]}. \tag{7}$$

The transport equations of $k$ and $\omega$ are defined as

$$\frac{\partial\rho k}{\partial t} + \frac{\partial}{\partial x_i}(\rho k\bar{u}_i) = \frac{\partial}{\partial x_j}\left[(\mu + \sigma_k\mu_t)\frac{\partial k}{\partial x_j}\right] + P_k - \beta^*\rho\omega k, \tag{8}$$

$$\begin{aligned}\frac{\partial\rho\omega}{\partial t} + \frac{\partial}{\partial x_i}(\rho\omega\bar{u}_i) &= \frac{\partial}{\partial x_j}\left[(\mu + \sigma_\omega\mu_t)\frac{\partial\omega}{\partial x_j}\right] + \frac{\rho\gamma}{\mu_t}P_k \\ &\quad -\beta\rho\omega^2 + 2\rho(1 - F_1)\frac{\sigma_{\omega,2}}{\omega}\frac{\partial k}{\partial x_j}\frac{\partial\omega}{\partial x_j},\end{aligned} \tag{9}$$

where $P_k$ represents the production of turbulence kinetic energy. It is modeled as

$$P_k = -\rho\overline{u_i'u_j'}\frac{\partial\bar{u}_i}{\partial x_j} \equiv \mu_t S^2 \tag{10}$$

with $S = \sqrt{2S_{ij}S_{ij}}$.

The different coefficients of the model, noted $\phi$, ($\phi = \{\sigma_k, \sigma_\omega, \beta, \gamma\}$), are defined by blending between the $k$–$\omega$ ($\phi_1$) and $k$–$\varepsilon$ ($\phi_2$) formulations in the form

$$\phi = F_1\phi_1 + (1 - F_1)\phi_2 \tag{11}$$

with

$$\begin{aligned}&\sigma_{k1} = 0.85, \quad \sigma_{\omega 1} = 0.5, \quad \beta_1 = 0.075, \quad a_1 = 0.31, \\ &\beta^* = 0.09, \quad \kappa = 0.41, \quad \gamma_1 = \beta_1/\beta^* - \sigma_{\omega 1}\kappa^2/\sqrt{\beta^*}\end{aligned}$$

and

$$\begin{aligned}&\sigma_{k2} = 1.0, \quad \sigma_{\omega 2} = 0.856, \quad \beta_2 = 0.0828, \\ &\gamma_2 = \beta_2/\beta^* - \sigma_{\omega 2}\kappa^2/\sqrt{\beta^*}.\end{aligned}$$

The blending functions $F_1$ and $F_2$ are defined as

$$\begin{aligned}F_1 &= \tanh\left(arg_1^4\right), \; F_2 = \tanh\left(arg_2^2\right), \\ arg_1 &= \min\left[\max\left(\frac{\sqrt{k}}{0.09\omega y}, \frac{500\mu}{\rho y^2\omega}\right), \frac{4\rho\sigma_{\omega,2}k}{CD_{k\omega}y^2}\right], \\ arg_2 &= \max\left[2\frac{\sqrt{k}}{0.09\omega y}, \frac{500\mu}{\rho y^2\omega}\right], \\ CD_{k\omega} &= \max\left[2\rho\sigma_{\omega,2}\frac{1}{\omega}\frac{\partial k}{\partial x_j}\frac{\partial\omega}{\partial x_j}, 10^{-20}\right].\end{aligned}$$

On the other hand, in the Reynolds stress model, Navier–Stokes equations are closed by solving directly the transport equations for the Reynolds stresses, together with an equation for the turbulent dissipation rate or the specific dissipation rate.[51] The first and most well-known fully developed RSM models are the Launder–Reece–Rodi (LRR)[52] and the Speziale–Sarkar–Gatski (SSG)[53] versions. In this paper, the baseline Reynolds stress model (BSL-RSM) variant was used. It is constructed based on the LRR model,[52] with a transport equation of the specific dissipation rate of the two-equation BSL model.[50] The exact transport equations for the Reynolds stresses can be written as follows:

$$\frac{\partial}{\partial t}\left(\rho\overline{u_i'u_j'}\right) + \frac{\partial}{\partial x_k}\left(\rho\bar{u}_k\overline{u_i'u_j'}\right) = D_{T,ij} + D_{L,ij} + P_{ij} + II_{ij} + \varepsilon_{ij}, \tag{12}$$

where $P_{ij}$ and $D_{L,ij}$ are, respectively, the stress production and the molecular diffusion terms, expressed as follows:

$$P_{ij} = -\rho\left(\overline{u_i'u_k'}\frac{\partial\bar{u}_j}{\partial x_k} + \overline{u_j'u_k'}\frac{\partial\bar{u}_i}{\partial x_k}\right), \tag{13}$$

$$D_{L,ij} = \frac{\partial}{\partial x_k}\left[\mu\frac{\partial}{\partial x_k}\left(\overline{u_i'u_j'}\right)\right], \tag{14}$$

and $\varepsilon_{ij}$ is the dissipation rate, $II_{ij}$, the pressure strain term, and $D_{Tij}$, the turbulent diffusion term. They are modeled as follows:[51]

$$\varepsilon_{ij} = -2\mu\overline{\frac{\partial u_i'}{\partial x_k}\frac{\partial u_j'}{\partial x_k}} \equiv -\frac{2}{3}\delta_{ij}\rho\beta^* k\omega, \tag{15}$$

$$\begin{aligned}II_{ij} = \overline{p'\left(\frac{\partial u_i'}{\partial x_j} + \frac{\partial u_j'}{\partial x_i}\right)} &\equiv -C_1\rho\beta^*\omega\left[\overline{u_i'u_j'} - \frac{2}{3}k\delta_{ij}\right] \\ &\quad -\hat{\alpha}_0\left[P_{ij} - \frac{1}{3}P_{kk}\delta_{ij}\right] - \hat{\beta}_0\left[D_{ij} - \frac{1}{3}P_{kk}\delta_{ij}\right] \\ &\quad -k\hat{\gamma}_0\left[S_{ij} - \frac{1}{3}S_{kk}\delta_{ij}\right],\end{aligned} \tag{16}$$

$$D_{Tij} = -\frac{\partial}{\partial x_k}\left[\rho\overline{u_i'u_j'u_k'} + \overline{p'\left(\delta_{kj}u_i' + \delta_{ik}u_j'\right)}\right] \equiv \frac{\partial}{\partial x_k}\left[\frac{\mu_t}{\sigma_k}\frac{\partial}{\partial x_k}\left(\overline{u_i'u_j'}\right)\right], \tag{17}$$

with

$$\begin{aligned}D_{ij} &= -\rho\left(\overline{u_i'u_m'}\frac{\partial\bar{u}_m}{\partial x_j} + \overline{u_j'u_m'}\frac{\partial\bar{u}_m}{\partial x_i}\right), \\ \hat{\alpha}_0 &= (8 + C_2)/11, \quad \hat{\beta}_0 = (8C_2 - 2)/11, \\ \hat{\gamma}_0 &= (60C_2 - 4)/55, \quad C_1 = 1.8, \quad C_2 = 0.52.\end{aligned}$$

In this study, simulations were performed using the $k$–$\omega$ SST and BSL-RSM versions implemented in ANSYS Fluent solver.[51] Furthermore, a $y^+$-insensitive type formulation is applied as a near-wall turbulence treatment model, $y^+$ being the dimensionless wall distance. This is defined by blending the viscous sublayer and the logarithmic layer formulations based on $y^+$. The non-dimensional near wall velocity profile, $u^+$, is expressed in the form[51]

$$\begin{cases} u^+_{blend} = f_u(u^+_{sub}, u^+_{log}), \\ u^+_{sub} = y^+, \\ u^+_{log} = \dfrac{1}{\kappa} ln(y^+) + C, \end{cases} \tag{18}$$

where $f_u$ is the blending function and $C$ is a log-layer constant.In a similar way, the value of $\omega$ is obtained as follows:

$$\begin{cases} \omega^+_{blend} = f_\omega(\omega^+_{sub}, \omega^+_{log}), \\ \omega^+_{sub} = \dfrac{6}{C_{\omega 2}\, y^{+2}}, \\ \omega^+_{log} = \dfrac{1}{\sqrt{C_\mu}\, y^+} \end{cases} \tag{19}$$

with $f_\omega$ being the blending function, and $C_{\omega 2}$ and $C_\mu$, the model constants.

Concerning the $k$-equation wall boundary condition, a zero flux condition is applied at the wall: $\frac{\partial k}{\partial n}|_{wall} = 0$, with $n$, the wall-normal coordinate.

### 2. Numerical setup

Simulations were performed on a heavy truck geometry identical to the experimental measurement configuration in the wind tunnel. The calculation domain was set according to the wind tunnel, with dimensions equivalent to the experimental test section dimensions, given in Fig. 6. However, the length downstream of the truck was extended to $29H$, to ensure that the flow is not disturbed downstream of the computational domain. No offset between the wheels and the ground was set in order to keep the same ground clearance between experiments and simulations.

The *inlet* was set in the domain's entry, with a mean velocity of 12 m s$^{-1}$ and a low turbulence intensity of 1%, in accordance with the turbulence intensity measured experimentally (Fig. 4). Downstream of the domain, boundary condition was set as *pressure outlet*. All side walls (lateral, top, and bottom walls) were assigned stationary *walls* boundary condition type. Simulations were run for 5 s with a time step of $10^{-3}$ s. For asymmetrical flows such as heavy truck recirculation region, it was found that the flow topology remains unchanged for time steps below $10^{-3}$ s.[22] Initially, simulations were run for 3.3 s, corresponding to 10 $T_f$, where $T_f$ is defined as the characteristic convective time it takes for a fluid particle to cover the domain length from the entrance to the exit. Then, simulations were run for an additional 5 $T_f$ ($\sim$1.7 s) for statistical data sampling.

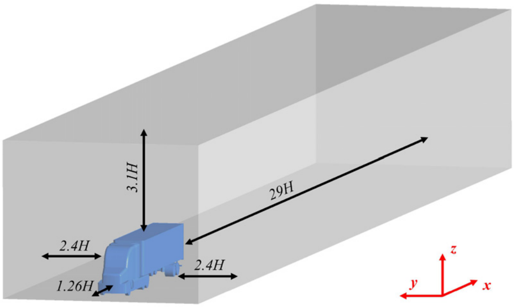

**FIG. 6.** Fluid computational domain and its dimensions.

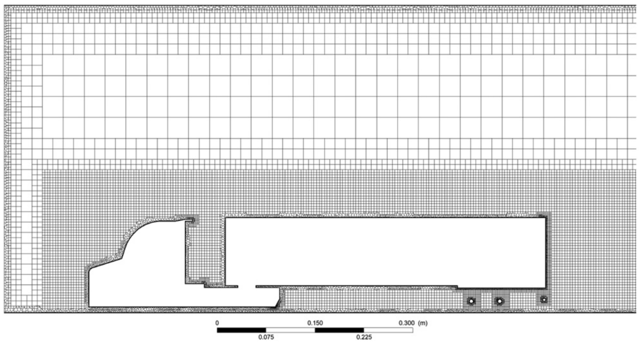

**FIG. 7.** Poly-hecxore mesh of 12*M* cells in the central longitudinal plane.

The mosaic poly-hexcore mesh from *Fluent Meshing* was generated. It consists of a structured mesh made of hexahedral cells away from the walls, and an unstructured mesh made of polyhedral cells in the near-wall regions (Fig. 7). This type of grid offers the advantage of reducing the total number of cells and thus the computation time, compared to tetrahedral, polyhedral, or hexagonal meshes, while maintaining a good mesh quality.[54] Ten inflation layers were applied to the walls with a growth rate of 1.15, to take into account boundary layers. The first layer thickness was fixed at 0.05 mm to guarantee a $y^+$ value within $\sim$1. A refined grid was applied to curved surfaces like wheels, trailer axles, stairs, and deflectors to ensure an acceptable mesh quality. A body of influence refinement method was applied around and in the wake of the heavy truck to obtain a refined mesh near the truck model (Fig. 7).

Three different meshes were generated by varying the cell size in the body of influence. Surface refinements and inflation parameters have not been modified between grids. The distribution of $y^+$ remains quite unchanged for the three meshes; $y^+$ is below 4.5 and around 1 for 99% of wall cells (Fig. 8). Mesh sensitivity, in a steady state

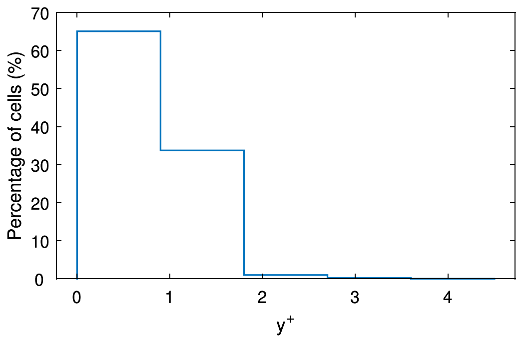

**FIG. 8.** $y^+$ distribution for the medium mesh. $y^+$ is around 1 for 99% of cells.

configuration, was performed between these three meshes: a coarse mesh, a medium mesh, and a fine mesh consisting of 3, 12, and 34 $\times 10^6$ cells, respectively. The normalized streamwise velocity $u/U_0$ and turbulent kinetic energy (TKE) $k$ profiles are given in Fig. 9 for the three meshes, obtained with the SST $k-\omega$ and the BSL-RSM models. Figure 9 shows similar velocity profiles for the three meshes and for both simulation models. However, turbulent kinetic energy profiles appear more scattered (Fig. 9), especially for those obtained with the BSL-RSM. For both first- and second-moment closure models, the coarse grid gives higher values of TKE than medium and fine meshes.

Differences between the different profiles were quantified using the normalized root mean square error (NRMSE), normalized by the difference between the maximum and minimum of the reference data [here, finest mesh data, or PIV measurements data in simulation-experiment comparison (Sec. III)]. NRMSE values of $u$ and $k$ are listed in Table II for comparison between coarse and medium grids (noted coarse–medium), and between medium and fine grids (noted medium–fine). NRMSE values obtained for the streamwise velocity profiles $u$ remain limited for both $k$–$\omega$ SST and BSL-RSM models and do not exceed 5% (Table II). This is not the case for TKE profiles, where the coarse mesh differs from the other grids. A larger but still limited NRMSE value is observed for both turbulence models, of around 10%. However, an important deviation is observed on TKE profiles obtained for the BSL-RSM between coarse and medium grids, with an NRMSE value of 26.6% (Table II).

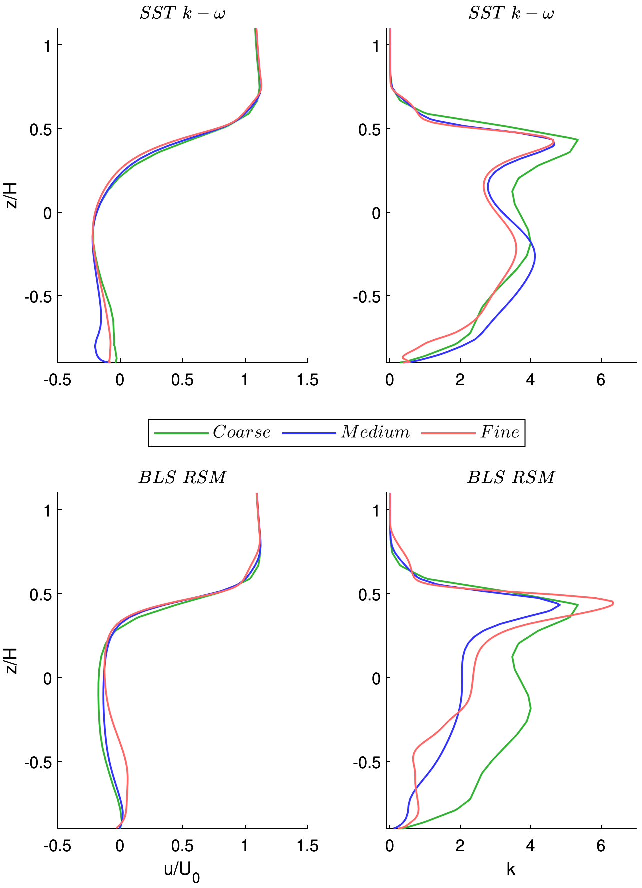

**FIG. 9.** Normalized streamwise velocity profiles and turbulent kinetic energy (TKE) on line $x = H$, for coarse, medium, and fine grids and for both turbulence models. Streamwise velocity profiles are similar for the three grids, whereas some differences appear on TKE profiles, especially between the coarse and other grids. These differences are more pronounced with the BSL-RSM.

**TABLE II.** Normalized root mean square errors between grids.

| | $u$ | | $k$ | |
|---|---|---|---|---|
| | $SST\ k-\omega$ | $BSL\text{–}RSM$ | $SST\ k-\omega$ | $BSL\text{–}RSM$ |
| Coarse–medium | 4.1% | 2.7% | 10.9% | 26.6% |
| Medium–fine | 3.1% | 4.3% | 9.5% | 8.1% |

For both turbulence models tested here, the medium mesh appears to be the best compromise between results accuracy and elements number, and thus calculation duration. The medium mesh of $12 \times 10^6$ cells, with a spatial resolution (grid size) in the wake of the heavy truck of $0.034H$, was, therefore, selected (Fig. 7).

Uncertainties associated with the choice of the turbulence closure model have been estimated considering all the turbulence models investigated in this study (*SST* $k-\omega$, *EARSM*, $\omega$ *RSM*, and *BSL-RSM*). The absolute relative deviations to the mean value of the four models computed for the four models are given in Table III, regarding global drag coefficient, and streamwise velocity and Reynolds stress components on profiles $x/H = \{0.25; 0.5; 0.75; 1; 1.25; 1.5\}$. As shown, relative deviations calculated for the drag coefficients and the streamwise velocity are low. The corresponding values are, respectively, less than 3.5 % and less than 1 %. However, they reach values over 30 % for the Reynolds stress components for both *SST* $k-\omega$ and $\omega$ *RSM* models.

## III. RESULTS

### A. Flow field

Simulation and PIV results of the normalized velocity magnitude and streamlines in the wake region are displayed in Fig. 10. The flow around the heavy truck is mainly characterized by a large pressure drop in the wake area.[55] Boundary layers formed along the truck surfaces separate at the edge corners contributing to the formation of a recirculation region.

The literature on heavy trucks aerodynamics[27,33–37,41] shows that airflow characteristics, including drag, turbulence, and pressure distribution, are highly dependent on the shape, size, and surface characteristics of the truck. The time-averaged drag coefficient returned by the two numerical models is, respectively, 0.578 ± 0.002 and 0.605 ± 0.002 for the SST $k-\omega$ and BSL-RSM models. Small variations in drag

**TABLE III.** Absolute relative deviations of the drag coefficient, velocity, and Reynolds stress, for the four tested turbulence models.

| | $SST\ k-\omega$ | $EARSM$ | $\omega\ RSM$ | $BSL\text{–}RSM$ |
|---|---|---|---|---|
| Drag coefficient | 3.3% | 3.3% | 1.3% | 1.3% |
| Streamwise velocity | 0.6% | 0.5% | 0.03% | 0.1% |
| Reynolds stress | 31.1% | 4.3% | 32.2% | 5.4% |

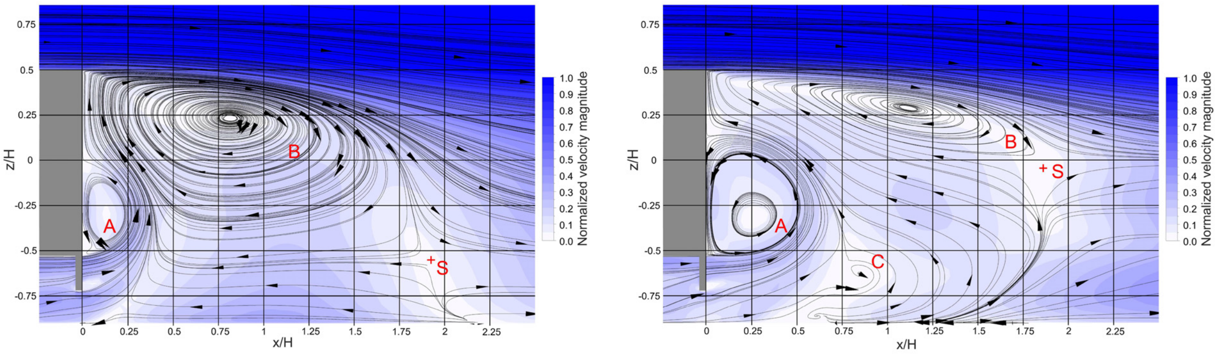

(a) Numerical, SST $k-\omega$

(b) Numerical, BSL-RSM

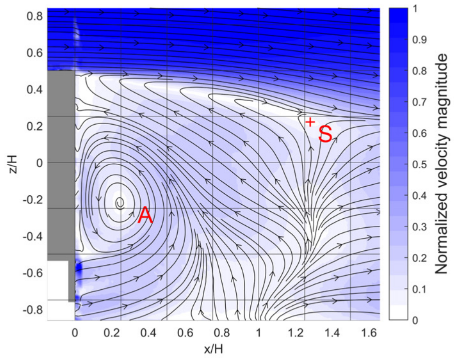

(c) Experimental

**FIG. 10.** Contours of velocity magnitude and streamlines in the wake of the heavy truck, in the vertical longitudinal midplane (*xz*), obtained numerically with the (a) SST $k-\omega$, (b) BSL-RSM, and (c) obtained experimentally. The gray area represents the trailer's back. Letters (A), (B), and (C) identify the three different vortices appearing in the recirculation region. Point (S) locates the saddle point. (A) vortex occurs on the three maps while (B) vortex only appears on numerical results.

coefficients of less than 0.4 % were observed during data statistical sampling. Drag coefficient values are quite similar to the one obtained by Taubert and Wygnanski,[41] which is 0.62, for a similar heavy truck geometry and at a close Reynolds number of $1.7 \times 10^5$.

For each studied case [Figs. 10(a)–10(c)], the flow separates in the upper back corner of the trailer, at $(x/H; z/H) = (0; 0.5)$, leading to the formation of a noticeable shear layer at the top of the recirculation region, called the upper shear layer.[40] For both numerical and experimental results [Figs. 10(a)–10(c)], a second shear layer (lower shear layer) with lower velocity gradients arises from the truck's sub-trailer $(x/H = 0; z/H < -0.5)$ and rolls up, leading to a counter-clockwise vortex (A) directly attached to the back of the truck. A saddle point (point S), described further in this section is visible in the three cartographies [Figs. 10(a)–10(c)]. The simulation and the experimental PIV results indicate significant differences in the size and shape of the "A" vortex structures (Fig. 10).

When focusing on streamlines, the size of the A vortex appears underestimated with the SST $k-\omega$ model as depicted in Fig. 10(a), compared to the experimental results [Fig. 10(c)]. The A vortex [Fig. 10(a)] fills less than the lower half of the trailer's height while its height is greater for the RSM model [Fig. 10(b)] and PIV measurements [Fig. 10(c)], and is, respectively, $0.65H$ and $0.75H$. The eddy turnover period obtained with the SST $k-\omega$ and BSL-RSM models was found to equal, respectively, 0.049 and 0.088 s, against 0.071 s for experiments results. The BSL-RSM approaches, thus, better the A vortex than the SST $k-\omega$ model, in comparison with the experimental results.

Streamlines indicate that an additional vortex (B), rotating clockwise and located at the top of the recirculation region, occurs in both numerical cartographies [Figs. 10(a) and 10(b)]. This "B" vortex is the result of the interaction between the upper shear layers and the A vortex described earlier.[40] The B vortex size differs considerably between the two RANS models [Figs. 10(a) and 10(b)]. For the SST $k-\omega$ model [Fig. 10(a)], the B vortex covers a large part of the recirculation region, reminding of a backward-facing step flow. This B vortex is more than three times smaller in height for the BSL-RSM model [Fig. 10(b)].

A third vortical structure (C) is also visible in the BSL-RSM model results [Fig. 10(b)], located in the lower part of the recirculation region. This structure originates from the lower part of the under-body of the heavy truck, more precisely from the recirculation zone formed behind the rear wheels. This airflow attached to the ground is driven by the airflow coming from both sides of the trailer and converging to the central mid-plane of the truck, which results in the formation of the "C" structure in the middle of the recirculation region.

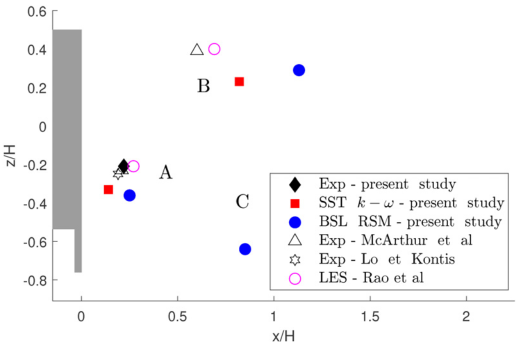

**FIG. 11.** Location of vortices centers obtained in the present study ($Re = 8.5 \times 10^4$) and in McArthur *et al.*[18] ($Re = 2.7 \times 10^4$), Lo and Kontis[40] ($Re = 6 \times 10^5$) and Rao *et al.*[20] ($Re = 2.7 \times 10^4$). (A) vortices centers appear localized while (B) vortices centers are more dispersed. (C) vortex only appears when using the BSL-RSM model.

A and B vortices have also been highlighted in existing studies on heavy-truck-like models, for Reynolds numbers ranging from $2.7 \times 10^4$ to $6 \times 10^5$.[18,19,22,23,25] The vortices center locations emerging from the present and previously cited studies are presented in Fig. 11. The A vortex center locations predicted in the present three cases are similar to those of the existing studies of McArthur *et al.*,[18] Lo and Kontis,[40] and Rao *et al.*,[20] given in Fig. 11, especially for PIV results. However, numerical RANS models tend to locate the A vortex center lower in the recirculation region, compared to experiments[18,40] and LES[20] (Fig. 11). The B vortex has already been observed in the wake flow of the GTS model.[18–20,22,23,25] B vortices centers are spatially scattered (Fig. 11), as simulation models used in the present study locate the B vortex center lower and further than experiments[18] and LES[20] in the recirculation region (Fig. 11).

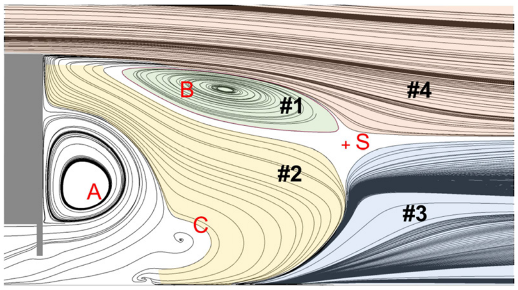

**FIG. 12.** Four zones identified in the wake of the heavy truck, obtained with the BSL-RSM.

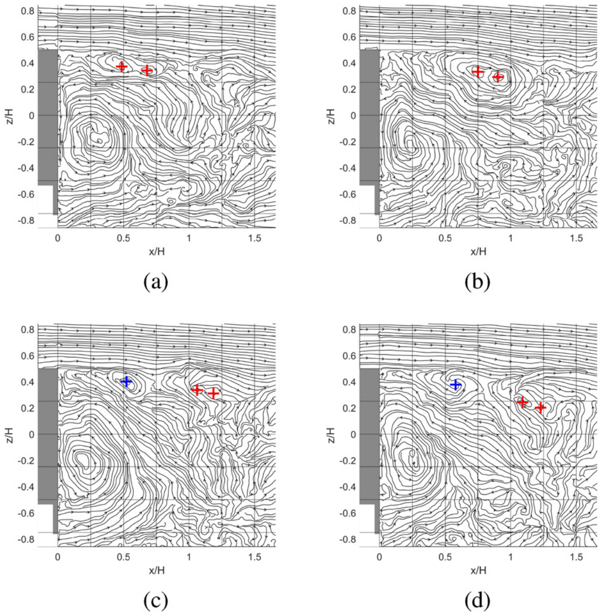

(a) (b) (c) (d)

**FIG. 13.** PIV instantaneous streamlines in the wake of the heavy truck, in the vertical longitudinal midplane (*xz*), for four consecutive snapshots: (a) $t = 7.400$ s, (b) $t = 7.467$ s, (c) $t = 7.533$ s, and (d) $t = 7.600$ s. Small vortices appear in the upper shear layer, identified by colored crosses.

From the simulation results [Figs. 10(a) and 10(b)], we can identify a saddle point "S," also observed by Ref. 18, dividing the flow into four parts (Fig. 12): part #1, containing the B vortex structure, part #2, where streamlines of negative streamwise velocity values circulate between the A and B vortices, part #3, outside of the recirculation region, where the flow of positive streamwise velocities is attached to the ground, and part #4, outside of the wake zone, where the flow directly comes from the top of the trailer. This point thus borders the recirculation region, where streamwise velocities are negatives, and thus directed toward the heavy truck. The saddle point is observed at, respectively, $(x/H; z/H) = (1.9; -0.55)$ and $(x/H; z/H) = (1.85; -0.04)$ in the SST $k-\omega$ [Fig. 10(a)] and BSL-RSM [Fig. 10(b)] models. For the BSL-RSM [Fig. 10(b)], its relative position to other vortices is qualitatively similar to that depicted by McArthur *et al.*[18] In the upper part of the recirculation region obtained experimentally [Fig. 10(c)], streamlines are highly curved and a saddle point is yet visible at $(x/H; z/H) = (1.28; 0.22)$, delimiting the recirculation region. The extent of the recirculation bubble is therefore highly overestimated by both numerical models compared to experiments, by approximately $x \sim 0.6H$, which is about 40 % of the mean length of the recirculation region.

Finally, we can notice that the B vortex structure observed numerically is not visible in the experimental PIV results of the mean velocity streamlines [Fig. 10(c)]. This can be explained by the unsteady character of the vortex-shedding flow. Indeed, flows in the wake of three-dimensional bluff bodies are known to be complex and highly unsteady,[28–32,56] and the time-averaging process of the wake flow obtained experimentally does not allow the observation of the B vortex. This can be verified by displaying snapshots of the instantaneous streamlines of four consecutive samples as presented in Fig. 13. The A vortex is visible in each of the four samples. Other small vortices, marked by the cross symbols in Fig. 13, are also visible in the upper shear layer. On Fig. 13(a), two vortices labeled by red crosses are located at $x/H = 0.49$ and $x/H = 0.68$. On Fig. 13(b), two equally spaced vortices appear $x \sim 0.25H$ further in the upper shear layer. These vortices seem to originate from vortex shedding due to the detachment of the flow at the trailer's rear top corner. One may assume that vortices marked by red crosses are in fact the same in Figs. 13(a) and 13(b). In this way, vortices labeled by a colored cross would be the same vortices convected by the upper shear layer. When vortices approach the saddle point, between $x/H = 1.2$ and $x/H = 1.3$ [red crosses, Figs. 13(c) and 13(d)], eddy structures tend to progressively break off, corresponding to the pumping phenomenon. Similar time-averaged and instantaneous flow topologies have been reported by Lo and Kontis.[40] According to Ref. 40, the upper shear layer interacts with the A vortex at the top of the recirculation region, which produces a flapping movement of the upper shear layer. In this way, the B vortex emerges and propagates along the upper shear layer, where it progressively disappears. Regrettably, experimental means used in the present study limit the PIV sampling frequency to 15 Hz ($St \sim 0.13$), whereas the vortex shedding characteristic Strouhal number, reported by Refs. 13 and 18 is around 0.19.

It should be noted that the issue of the B vortex only appearing on numerical results, compared to experimental results, has already been reported by Refs. 13 and 42, who studied a realistic heavy truck geometry using LES, in comparison with the PIV study of Lo and Kontis.[40]

### B. Velocity profiles

Figure 14 shows a comparison between numerical and experimental streamwise mean velocity profiles downstream of the truck model, at $x = 0.25H$, $x = 0.5H$, $x = 0.75H$, $x = H$, $x = 1.25H$, and $x = 1.5H$. Error bars of PIV data are displayed, corresponding to $\mathscr{U}_{\bar{u}}$, computed using Fig. 2. It can be seen that there is a fairly good agreement between simulations and experiments. Gray vertical lines $u/U_0 = 0$ help to distinguish negative from positive velocities.

In the recirculation region $(-0.5 \leq z/H \leq 0.5)$, most numerical profiles present negative values of the streamwise velocity, corresponding to the recirculation region located upstream of the saddle point. Experimental data show negative velocities for the first four profiles $(x/H = \{0.25; 0.5; 0.75; 1\})$, velocities around zero on profile $x = 1.25H$, and positive velocities on the last profile $x = 1.5H$. This is consistent with the previous description in Fig. 10(c), where the saddle point obtained with PIV ($S_{exp}$ on Fig. 14) is observed around $x/H = 1.28$, corresponding to the end of the recirculation region. Numerical simulations return negative streamwise velocities for $-0.5 \leq z/H \leq 0.5$ and up to $x = 1.5H$. Streamwise velocities of the last two profiles are highly undervalued compared with experiments, as they are outside the error bars. The previous observation based on the mean flow cartographies (Fig. 10), concerning the overestimation of the recirculation region extent obtained with both numerical models, is confirmed, considering the velocity profiles (Fig. 14).

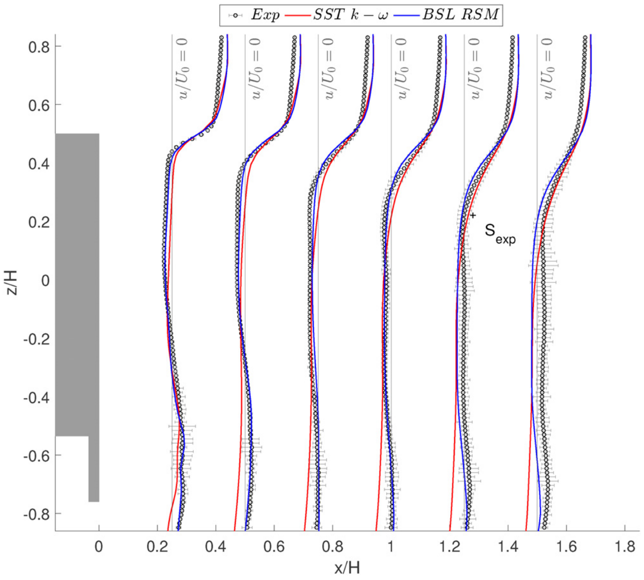

**FIG. 14.** Normalized streamwise ($x-$) velocity on vertical lines in plane ($xz$), in the wake of the heavy truck. The gray area represents the trailer's back. The first four profiles show a good agreement between experiments and simulation. The two last profiles show a slightly lower accordance, especially for the SST $k-\omega$.

The BSL-RSM model reproduces properly the shape of velocity distribution profiles either in the lower part $(z/H \leq -0.5)$ as well as in the whole recirculation region $(-0.5 \leq z/H \leq 0.5)$, for profiles $x = 0.25H$, $x = 0.5H$, $x = 0.75H$ and $x = H$, where the streamwise velocity profiles are quite identical. Some differences are visible on profiles $x = 1.5H$, which is related to the large extent of the recirculation zone predicted by the BSL-RSM model in comparison with PIV experiments. The SST $k$–$\omega$ model, on the other hand, shows significant discrepancies in the near-ground region. In the lower part of the velocity profiles $(z/H \leq -0.5)$, where error bars are larger, streamwise velocities obtained with the SST $k-\omega$ model are negative in comparison with the BSL-RSM model and experimental results which are positive. As observed in Fig. 10(a), the SST $k-\omega$ model does not reproduce well the lower part of the recirculation region obtained experimentally, where the flow attached to the ground has negative streamwise velocity components. Note that in the published papers of Wang *et al.*[13] and Xie *et al.*,[42] the application of LES for simulating the flow behind a realistic truck also showed noticeable differences when comparing the mean velocity profiles with the experimental measurement results reported by Lo and Kontis.[40]

The BSL-RSM shows an overall better agreement with experiments than the SST $k-\omega$ model, especially for profiles $x/H = \{0.25; 0.5; 0.75; 1\}$. The corresponding NRMSE values vary between 5.3% and 6.3%, while for the SST $k-\omega$ model; they vary between 9.1% and 12.7%. However, differences between experiments and simulations increase when advancing in the wake flow. Indeed, for the velocity profile $x = 1.5H$, the NRMSE value exceeds 20% for both numerical models, which is related to the difference in the size of the predicted recirculation zone. Differences between numerical and experimental results remain overall relatively limited, particularly in the case of the BSL-RSM model where velocity profiles are in good agreement with PIV results, especially for profiles $x/H = \{0.25; 0.5; 0.75; 1\}$. To confirm this, profiles of fluctuated velocity correlations are investigated in Sec. III C.

### C. Reynolds stresses

In Fig. 15, a comparison between THE numerical and experimental results of the Reynolds stress components, normalized relative to the freestream velocity, IS presented along six vertical profiles $x = 0.25H$, $x = 0.5H$, $x = 0.75H$, $x = H$, $x = 1.25H$, and $x = 1.5H$.

In Fig. 15(a), the streamwise turbulence intensity returned by the numerical models is reasonably in good agreement in the shear layer region $(0.25 \leq z/H \leq 0.5)$ and generally in the upper part of the

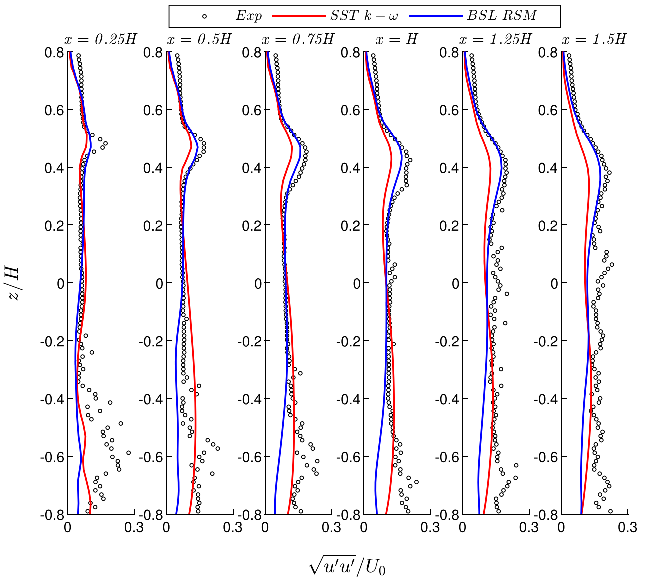

(a) Streamwise Reynolds Stress component

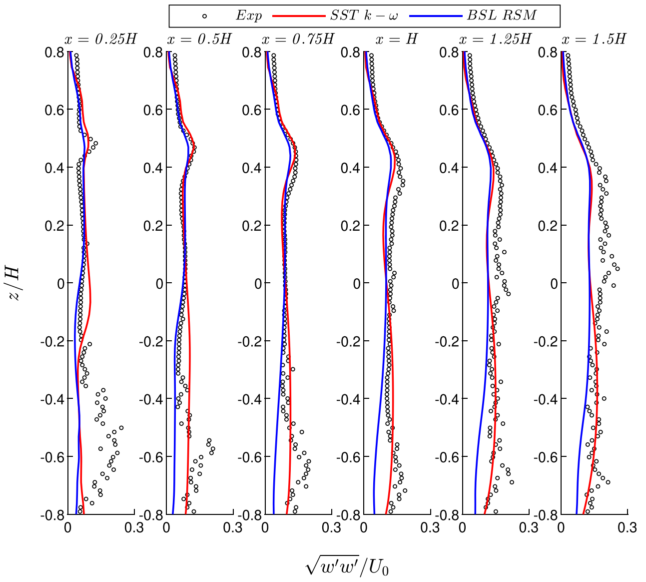

(b) Spanwise Reynolds Stress component

**FIG. 15.** Normalized (a) streamwise and (b) spanwise Reynolds Stress components on vertical lines $x/H = \{0.25; 0.5; 0.75; 1; 1.25; 1.5\}$. The overall trend of experimental Reynolds stresses is reproduced by both numerical models. However, notable differences between PIV and simulation results are measured near the ground, where the turbulent intensity values almost reach 30%.

vertical profiles $(z/H \geq 0)$. The maximum level of the turbulence intensity is of the order of 20%, which corresponds to the region of turbulent kinetic energy production due to the important streamwise velocity gradients, that is in the upper shear layer $(0.25 \leq z/H \leq 0.5)$. Except for the first profile, the BSL-RSM model appears to reproduce well the turbulence intensity peaks of experimental results in comparison with the SST $k$–$\omega$ model where peaks are slightly underestimated. In the bottom part of the turbulence intensity profiles $(z/H \leq 0)$, discrepancies between numerical and experimental results are pronounced, especially for the $x = 0.25H$ profile. The measured turbulence intensity is considerably high near the back truck tail $(z/H \leq -0.3)$ which is reasonable given the bounded region within the ground and the back truck walls. The SST $k$–$\omega$ model seems to be relatively more consistent with PIV than the BSL-RSM model to predict the streamwise Reynolds stress component in the lower part of the wake flow, but the differences are significant in some points. The NRMSE are relatively high, approximately 27% in all profiles for the BSL-RSM model, while it varies, for the SST $k$–$\omega$, between 18% and 23% in the first five profiles, and it reaches 28% in profile $x = 1.5H$.

In Fig. 15(b), similar comments as in the streamwise turbulence intensity profiles can be made, in the case of the spanwise turbulence intensity component. In the upper part, both the BSL-RSM and SST $k$–$\omega$ models are consistent with the PIV results, especially for profiles $x/H = \{0.5; 0.75; 1\}$. The level of turbulence exceeds 15 % along the shear stress layer $(0.25 \leq z/H \leq 0.5)$. In the bottom part $(z/H \leq 0)$, the two turbulence models predict no satisfactory results. The $k$–$\omega$ SST model returns reasonably the correct level of turbulence intensity for profiles $x/H = \{0.75; 1; 1.25; 1.5\}$, unlike the BSL-RSM model where the level of turbulence is underestimated in all profiles. The corresponding NRMSE values are about 29% in the back truck closest profile and vary between 14% and 19% in the other profiles of the SST $k$–$\omega$ model. In the BSL-RSM model, NRMSE values are between 21% and 31%.

However, one must keep in mind that the limitations of numerical models in predicting the experimental results of the turbulence intensity must be nuanced given the relevance of the PIV measurement technique used in this study, where the acquisition frequency of 15 Hz may not be sufficient to measure the fluctuating turbulent quantities. Considering the results presented in Secs. III A–III C, that are flow field, velocity profiles, and Reynolds stresses profiles, the BSL-RSM approaches the experimental results of the flow in the wake of a heavy truck better than the SST $k-\omega$ model. Nevertheless, other quantities, such as vortex identification criteria, must be investigated to confirm this finding.

## D. Identification of coherent vortical structures

The previous results (Sec. III A) have highlighted the topology of the wake flow of the simplified heavy truck, through the streamline patterns. Two counter-rotating vortices are observed with both RANS-models [Figs. 10(a) and 10(b)] whereas a single counterclockwise vortex appears on the time-averaged flow field obtained by PIV [Fig. 10(c)]. On the other hand, the instantaneous streamlines (Fig. 13) indicate that vortex shedding may occur in the upper shear layer. However, these results are not sufficient to affirm the existence of eddy structures described in Sec. III A. For a more detailed analysis of vortex structures in the wake flow, other identification methods are considered in the following.

According to Hunt *et al.*,[57] vortical structures are defined as strong swirling zones with non-zero vorticity. Two criteria allow for characterizing these flow regions. The first criterion is that the irrotational straining is small compared with the vorticity, and the second criterion is defined by a minimum local pressure in the vortex center.

There exist various methods allowing the identification of vortical structures in turbulent flows. In Sec. III A, eddy structures were identified by considering closed spiraling streamlines of a time-averaged velocity field. This method is consistent with the detection approach reported by Lugt,[58] who suggested examining regions of closed streamlines in different time-sequence of instantaneous streamline patterns and making sure that their center's locations do not move relative to their respective reference. This approach, however, may not be the appropriate technique to use in complex three-dimensional flows because the vortex core is not Galilean invariant, and may appear not appropriate to identify vortex in a turbulent flow containing numerous vortices advecting at different speeds.[59] Visualization of the local minimum pressure is also commonly used as an indicator to determine the vortex core region,[59,60] as well as the maximum vorticity magnitude, which seems to be a pertinent technique for the identification of vortex structures.[61–63]

Methods based on Galilean invariants have been developed for the identification of vortex structures by using the invariants of the velocity gradient tensor $\nabla \mathbf{u}$. Chong *et al.*[64] identified the core vortex as a region with complex eigenvalues $\sigma$ satisfying the characteristic equation,

$$\sigma^3 - P\sigma^2 + Q\sigma - R = 0, \tag{20}$$

where the invariants $P$, $Q$ and $R$ are defined as

$$P \equiv \frac{\partial u_i}{\partial x_i} = 0, \tag{21a}$$

$$Q \equiv \frac{1}{2}\left(\frac{\partial u_i}{\partial x_i}\frac{\partial u_i}{\partial x_i} - \frac{\partial u_i}{\partial x_j}\frac{\partial u_j}{\partial x_i}\right), \tag{21b}$$

$$R = det\left(\frac{\partial u_i}{\partial x_j}\right). \tag{21c}$$

Hunt *et al.*,[57] on the other hand, defined the vortex structure as a region with a positive second invariant $Q$, which can be expressed by the following equation:[59]

$$Q \equiv \frac{1}{2}\left(\frac{\partial u_i}{\partial x_i}\frac{\partial u_i}{\partial x_i} - \frac{\partial u_i}{\partial x_j}\frac{\partial u_j}{\partial x_i}\right) = -\frac{1}{2}\left(\frac{\partial u_i}{\partial x_j}\frac{\partial u_j}{\partial x_i}\right)$$
$$= \frac{1}{2}\left(||\Omega||^2 - ||\mathbf{S}||^2\right), \tag{22}$$

where $||\mathbf{S}|| = \sqrt{tr(\mathbf{S}\mathbf{S}^t)}$, $||\Omega|| = \sqrt{tr(\Omega\Omega^t)}$, and $\mathbf{S}$ and $\Omega$ are, respectively, the symmetric (strain-rate tensor) and antisymmetric (vorticity tensor) components of $\nabla \mathbf{u}$. Thus, $Q$ represents the local balance between vorticity and shear strain rate magnitude.

In the following, two techniques of identification of vortex structures, i.e., the vorticity magnitude, and the Q-criterion-based methods,

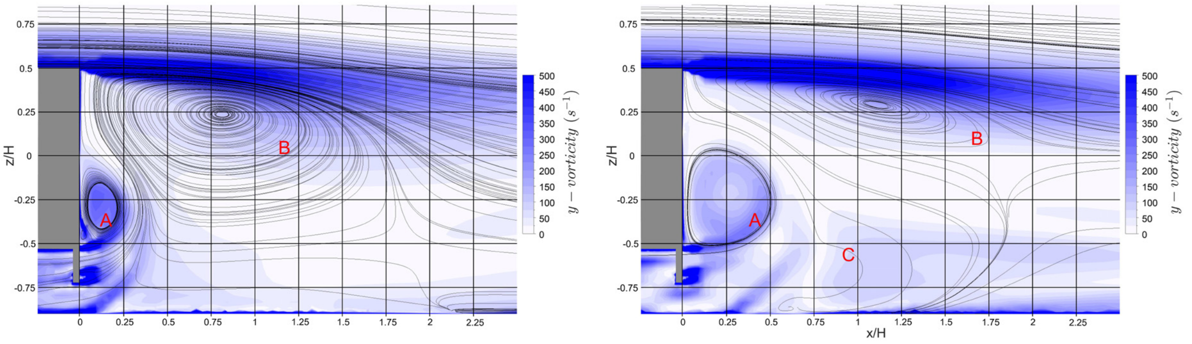

(a) Numerical, SST $k-\omega$

(b) Numerical, BSL-RSM

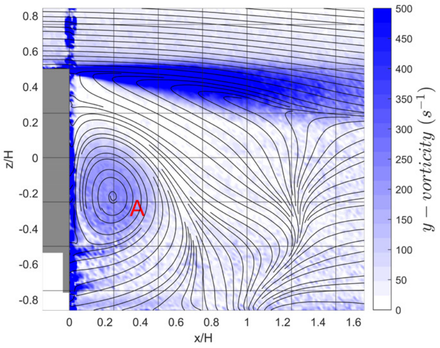

(c) Experimental

**FIG. 16.** Spanwise *y*-vorticity magnitude and streamlines in the wake of the heavy truck, in the vertical midplane (*xz*), obtained numerically with the (a) SST $k-\omega$, (b) BSL-RSM, and (c) obtained experimentally. The gray area represents the trailer's back. Letters (A), (B), and (C) stand for vortices identified by streamlines. Highest values of vorticity are observed in the upper shear layer.

are examined by analyzing numerical and PIV results in the wake of the heavy truck. Figures 16 and 17 show, respectively, contours of the $y$-vorticity magnitude and Q-criterion in the longitudinal vertical plane, behind the truck, obtained with the SST $k-\omega$ model, the BSL-RSM model, and with experiments.

In Fig. 16, it can be seen that the two turbulence models and PIV results display some resemblance in the vorticity contours. The vorticity produced on the truck surfaces is spreading into the wake region. Under the truck, high values of vorticity magnitude indicate that vortical structures are produced into the wake flow, resulting in the A vortex, which expands by the vortex stretching mechanism. This vortex is well identified in the three contours with some difference in the size of the vortex predicted by the $k$–$\omega$ SST model [Fig. 16(a)], which appears shrunken. This is consistent with previous results of streamlines presented in Sec. III A (Fig. 10). On the upper part, an elongated vorticity region covers the shear layer zone referred to as the vortex shedding zone. This is well illustrated by the high values in the vorticity magnitude. However, neither in the simulation nor on experiments contours, the upper vortex core (the observed B vortex on streamlines) is well identified. Finally, the vorticity produced in the near-ground boundary layer is also visible for the three contours (Fig. 16).

Visualization of the Q-criterion results Fig. 17, on the other hand, allows identifying vortex core regions characterized by high values of the Q-criterion. Two distinct regions of vortical structures appear and are quasi-identical in the numerical [Figs. 17(a) and 17(b)] and experimental results [Fig. 17(c)]. The A vortex is well illustrated, with some resemblance, particularly between the BSL-RSM model [Fig. 17(b)] and PIV results [Fig. 17(c)]. This vortex is also visible in the $k$–$\omega$ SST model [Fig. 17(a)] but it seems shrunken and less elevated. The second region of vortical structures identified by the Q-criterion is the shear layer region, where vorticity is produced at the top corner of the truck surface and propagates into the wake region as a shear flow with vortices. An important difference is reported in the PIV results [Fig. 17(c)] where it can be noticed that distinct vortex cores are well identified, unlike the numerical models where only the separation at the top corner of the truck is detected.

Also unlike the vorticity magnitude visualization method, the Q-criterion allows excluding regions with relatively high vorticity, where no vortex occurs: in the ground boundary layer, in the under-trailer, and in the whole upper shear layer. Q-criterion, thus, provides an important advantage over vorticity magnitude, particularly when the background shear is comparable to the vorticity magnitude within the vortex as reported by Jeong and Hussain.[59] Finally, it can be pointed out that identifying vortical structures exclusively on the basis of streamlines does not seem suitable. Indeed, despite the correct identification of the A vortex, the identification of the upper shear layer region as a second vortex does not appear pertinent. In this case, the use of the Q-contours method is preferred. The vorticity magnitude-

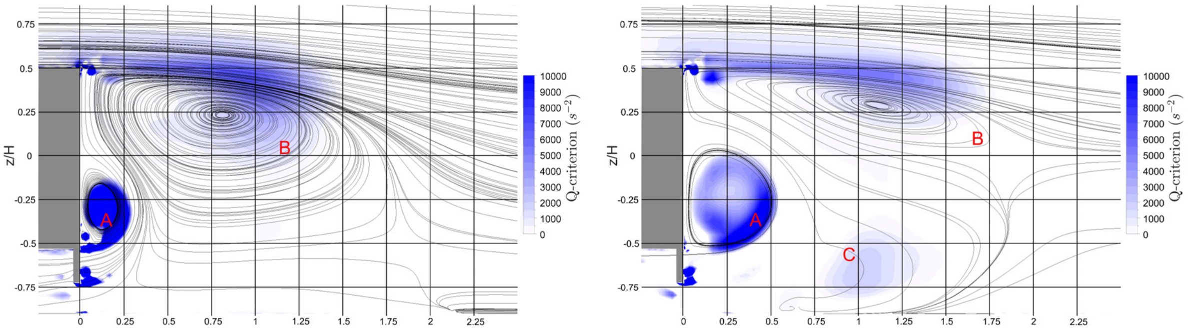

(a) Numerical, SST $k-\omega$

(b) Numerical, BSL-RSM

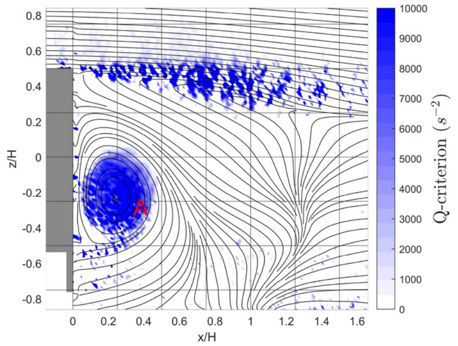

(c) Experimental

**FIG. 17.** Q-criterion and streamlines in the wake of the heavy truck, in the vertical midplane ($xz$), obtained numerically with the (a) SST $k-\omega$, (b) BSL-RSM and (c) obtained experimentally. The gray area represents the trailer's back. Letters (A), (B), and (C) stand for vortices identified by streamlines. Q-criterion maxima clearly identify the (A) vortex and vortices occurring in the upper shear layer.

based technique, on the other hand, appears appropriate in this case but it may present some limitations in the case of wall-bounded flows since it tends to highlight the background shear too.

Finally, in order to get a general overview of the vortex structures developing around the truck body, a three-dimensional visualization of the vortex structures prevalent in the mean flow is shown in Fig. 18, obtained with the BSL-RSM simulation model, using Q-criterion isosurfaces and colored by the velocity magnitude, normalized by $U_0$. It can be observed that when the flow encounters the front of the truck, it is forced to separate from the body and forms a low-pressure region. This separation leads to the formation of large vortices that trail behind the truck and in the intermediate gap, between the tractor and the trailer. At the front, the flow is deflected to the sides and longitudinal vortex structures are driven along the sides of the truck. In addition, near the wheels, vortex structures are visible. This is the result of the interaction of the flow with under-body elements. On the trailer truck, small vortices with low velocities are observed over the entire surface of the trailer.

## IV. CONCLUSION

The wake flow of a 1:28 reduced-scale heavy truck model was investigated at $Re = 8.5 \times 10^4$ using numerical simulations supported by PIV measurements in a wind tunnel configuration. Simulations were based on resolving the Navier–Stokes equations in a URANS-based approach with two closure turbulence models, namely the SST $k - \omega$ and BSL-RSM models.

The wake flow is characterized by the existence of different vortex structures:

- A core vortex arising from the under-trailer (A vortex) is attached to the back wall of the truck. This latter's height is found to be, respectively, 0.65 and 0.75 the height of the truck's trailer, for the BSL-RSM model and the PIV results, while for the $k$–$\omega$ SST, it is less than the half.
- A notable shear layer region developing from the upper corner of the trailer appears in the top of the recirculation region. The analysis of the instantaneous streamlines obtained by PIV measurements has highlighted the occurrence of vortex shedding in the upper recirculation region.
- A saddle point has been observed, lying in a region of zero velocity magnitude and demarcating the end of the recirculation region. This region extent is over $1.85H$ in the simulations, against $1.28H$ in the experiments.

The application of both vorticity magnitude and $Q$-invariant maximal values-based methods of vortex structures identification have highlighted that:

- Visualization of streamlines does not appear to be a reliable vortex identification technique, as streamlines obtained numerically revealed the occurrence of a second vortex located near the upper shear layer (B vortex).
- Q-criterion contours yield a better representation of vortex structures locations than vorticity magnitude, as zones of high shear layer appear with high values of vorticity magnitude while they are filtered by the Q-invariant.

The confrontation of the two URANS models compared with experiments, regarding time-averaged streamwise velocity and Reynolds stresses profiles, streamlines, contours of vorticity, and of Q-criterion, revealed that:

- URANS approach leads to a reasonable representation of the wake flow observed in the experimental measurements using PIV, as coherent structures are identified by the Q-criterion for both numerical models.
- Overall, the BSL-RSM shows a better prediction of experimental results. Regarding streamwise velocity profiles, the NRMSE values are, respectively, less than 6% for the BSL-RSM, against 13% for the SST $k - \omega$, for $x/H < 1.25$.

However, RANS models have shown some limitations especially:

- The recirculation region extent is overestimated by ∼40% by numerical simulations, compared to experiments.
- Both URANS models fail to give correct values of streamwise and spanwise Reynolds stress components. The global NRMSE on Reynolds stress profiles, between simulations and experiments, exceeds 20%.

The wake flow of a realistic heavy truck is thus complex with eddy structures of different scales and dynamics that may influence

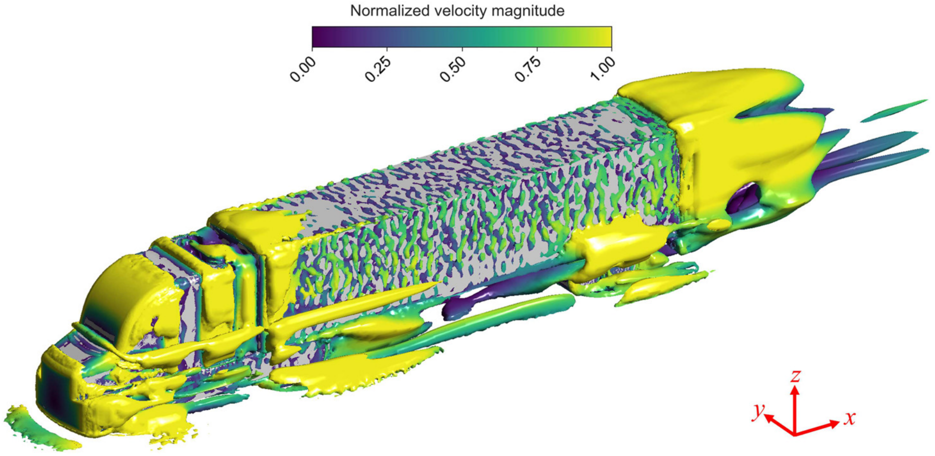

**FIG. 18.** Isocontour of Q-criterion colored by normalized velocity magnitude around the heavy truck, obtained with the BSL-RSM, revealing the coherent structures prevalent in the mean flow. The most noticeable eddy structures are located in the under-body and in the wake of the heavy truck.

highly the dispersion of pollutants. The next step will consist in modeling the dynamics of the pollutants originating from the exhaust pipes in order to understand and develop new strategies to improve the air quality related to road traffic. To complete the experimental part of this study, further measurements using a higher sampling frequency, using, for example, time resolved-PIV, would be required to identify properly the unsteady characteristics of the flow, especially the vortex shedding occurring in the upper recirculation region, evidenced in the literature. This phenomenon could strongly affect the emergence of the B vortex revealed by CFD simulations.

## ACKNOWLEDGMENTS

The authors would like to express their gratitude to ESTACA'LAB for the funding of this project and for providing the necessary experimental and computational resources. The authors also gratefully acknowledge David Perez for his significant contribution to the experimental setup and for his valuable assistance.

## AUTHOR DECLARATIONS

### Conflict of Interest

The authors have no conflicts to disclose.

### Author Contributions

**Aude Pérard-Lecomte:** Conceptualization (lead); Data curation (lead); Formal analysis (lead); Investigation (lead); Methodology (lead); Software (lead); Validation (lead); Visualization (lead); Writing – original draft (lead); Writing – review & editing (equal). **Mokhtar Djeddou:** Conceptualization (equal); Formal analysis (lead); Investigation (equal); Methodology (lead); Software (lead); Writing – original draft (lead); Writing – review & editing (equal). **Georges Fokoua:** Conceptualization (equal); Formal analysis (equal); Methodology (equal); Project administration (equal); Supervision (equal); Validation (equal); Writing – review & editing (equal). **Amine Mehel:** Conceptualization (equal); Formal analysis (equal); Project administration (equal); Supervision (equal); Validation (equal); Writing – review & editing (equal). **Anne Tanière:** Conceptualization (equal); Formal analysis (equal); Methodology (equal); Project administration (equal); Supervision (equal); Validation (equal); Writing – review & editing (equal).

## DATA AVAILABILITY

The data that support the findings of this study are available from the corresponding author upon reasonable request.

## REFERENCES

[1] C. Buzea, I. I. Pacheco, and K. Robbie, "Nanomaterials and nanoparticles: Sources and toxicity," Biointerphases **2**, MR17–MR71 (2007).

[2] C. A. Pope Iii, R. T. Burnett, M. J. Thun, E. E. Calle, D. Krewski, K. Ito, and G. D. Thurston, "Lung cancer, cardiopulmonary mortality, and long-term exposure to fine particulate air pollution," JAMA **287**, 1132–1141 (2002).

[3] World Health Organization, *Health Effects of Particulate Matter: Policy Implications for Countries in Eastern Europe, Caucasus and Central Asia* (World Health Organization, 2013).

[4] F. Sommer, V. Dietze, A. Baum, J. Sauer, S. Gilge, C. Maschowski, R. Gieré *et al.*, "Tire abrasion as a major source of microplastics in the environment," Aerosol Air Qual. Res. **18**, 2014–2028 (2018).

[5] L. J. Knight, F. N. Parker-Jurd, M. Al-Sid-Cheikh, and R. C. Thompson, "Tyre wear particles: An abundant yet widely unreported microplastic?," Environ. Sci. Pollut. Res. **27**, 18345–18354 (2020).

[6] O. Oussairan, E. Varea, G. Fokoua, B. Patte-Rouland, and F. Murzyn, "Interaction between two car models with application to pollutant dispersion," Exp. Therm. Fluid Sci. **143**, 110815 (2023).

[7] L. I. Zaichik, V. M. Alipchenkov, and E. G. Sinaiski, *Particles in Turbulent Flows* (John Wiley and Sons, 2008).

[8] M. Caporaloni, F. Tampieri, F. Trombetti, and O. Vittori, "Transfer of particles in nonisotropic air turbulence," J. Atmos. Sci. **32**, 565–568 (1975).

[9] M. Reeks, "The transport of discrete particles in inhomogeneous turbulence," J. Aerosol Sci. **14**, 729–739 (1983).

[10] K. D. Squires and J. K. Eaton, "Preferential concentration of particles by turbulence," Phys. Fluids A: Fluid Dyn. **3**, 1169–1178 (1991).

[11] W. C. Reade and L. R. Collins, "Effect of preferential concentration on turbulent collision rates," Phys. Fluids **12**, 2530–2540 (2000).

[12] C. Marchioli, *Collective Dynamics of Particles: From Viscous to Turbulent Flows* (Springer, 2017), Vol. 576.

[13] F. Wang, C.-H. Liu, and J. Xie, "Wake dynamics and pollutant dispersion behind a light-duty lorry," Phys. Fluids **33**, 095127 (2021).

[14] S. R. Ahmed, G. Ramm, and G. Faltin, "Some salient features of the time-averaged ground vehicle wake," SAE Trans. **93**, 473–503 (1984).

[15] H. Lienhart, C. Stoots, and S. Becker, "Flow and turbulence structures in the wake of a simplified car model (Ahmed model)," in *New Results in Numerical and Experimental Fluid Mechanics III* (Springer, 2002), pp. 323–330.

[16] E. Serre, M. Minguez, R. Pasquetti, E. Guilmineau, G. B. Deng, M. Kornhaas, M. Schäfer, J. Fröhlich, C. Hinterberger, and W. Rodi, "On simulating the turbulent flow around the Ahmed body: A French–German collaborative evaluation of LES and DES," Comput. Fluids **78**, 10–23 (2013).

[17] B. L. Storms, J. C. Ross, J. T. Heineck, S. M. Walker, D. M. Driver, G. G. Zilliac, and D. P. Bencze, "An experimental study of the ground transportation system (GTS) model in the NASA ames 7-by 10-ft wind tunnel," Technical Report No. NASA/TM-2001-209621 (NASA Center for AeroSpace Information, 2001).

[18] D. McArthur, D. Burton, M. Thompson, and J. Sheridan, "On the near wake of a simplified heavy vehicle," J. Fluids Struct. **66**, 293–314 (2016).

[19] T. Castelain, M. Michard, M. Szmigiel, D. Chacaton, and D. Juvé, "Identification of flow classes in the wake of a simplified truck model depending on the underbody velocity," J. Wind Eng. Ind. Aerodyn. **175**, 352–363 (2018).

[20] A. N. Rao, J. Zhang, G. Minelli, B. Basara, and S. Krajnović, "An LES investigation of the near-wake flow topology of a simplified heavy vehicle," Flow Turbul. Combust. **102**, 389–415 (2019).

[21] J. M. Ortega, T. Dunn, R. McCallen, and K. Salari, "Computational simulation of a heavy vehicle trailer wake," in *The Aerodynamics of Heavy Vehicles: Trucks, Buses, and Trains* (Springer, 2004), pp. 219–233.

[22] J. Zhang, Z. Guo, S. Han, S. Krajnović, J. Sheridan, and G. Gao, "An IDDES study of the near-wake flow topology of a simplified heavy vehicle," Transp. Safety Environ. **4**, tdac015 (2022).

[23] J. Zhang, F. Wang, Z. Guo, S. Han, G. Gao, and J. Wang, "Investigation of the wake flow of a simplified heavy vehicle with different aspect ratios," Phys. Fluids **34**, 065135 (2022).

[24] C. J. Roy, J. Payne, and M. McWherter-Payne, "RANS simulations of a simplified tractor/trailer geometry," J. Fluids Eng. **128**, 1083–1089 (2006).

[25] A. N. Rao, G. Minelli, J. Zhang, B. Basara, and S. Krajnović, "Investigation of the near-wake flow topology of a simplified heavy vehicle using PANS simulations," J. Wind Eng. Ind. Aerodyn. **183**, 243–272 (2018).

[26] W. T. Gutierrez, B. Hassan, R. H. Croll, and W. H. Rutledge, "Aerodynamics overview of the ground transportation systems (GTS) project for heavy vehicle drag reduction," Technical Report No. 960204-2 (Sandia National Laboratory (SNL-NM), Albuquerque, NM, 1995).

[27] J. T. Heineck, S. M. Walker, and D. Satran, "The measurement of wake and gap flows of the generic conventional truck model (GCM) using three-component PIV," in *The Aerodynamics of Heavy Vehicles: Trucks, Buses, and Trains* (Springer, 2004), pp. 173–184.

[28] G. Bonnavion and O. Cadot, "Unstable wake dynamics of rectangular flat-backed bluff bodies with inclination and ground proximity," J. Fluid Mech. **854**, 196–232 (2018).

[29] M. Grandemange, M. Gohlke, and O. Cadot, "Bi-stability in the turbulent wake past parallelepiped bodies with various aspect ratios and wall effects," Phys. Fluids **25**, 095103 (2013).

[30] E. G. Duell and A. George, "Experimental study of a ground vehicle body unsteady near wake," SAE Trans. **108**, 1589–1602 (1999).

[31] D. Fan, B. Zhang, Y. Zhou, and B. R. Noack, "Optimization and sensitivity analysis of active drag reduction of a square-back Ahmed body using machine learning control," Phys. Fluids **32**, 125117 (2020).

[32] B. Podvin, S. Pellerin, Y. Fraigneau, A. Evrard, and O. Cadot, "Proper orthogonal decomposition analysis and modelling of the wake deviation behind a squareback Ahmed body," Phys. Rev. Fluids **5**, 064612 (2020).

[33] I. Bayraktar, D. Landman, W. K. Cary, R. Wood, J. Flamm, and C. Hunter, "An assessment of drag reduction devices for heavy trucks using design of experiments and computational fluid dynamics," SAE Trans. **114**, 135–146 (2005).

[34] D. Landman, R. Wood, W. Seay, and J. Bledsoe, "Understanding practical limits to heavy truck drag reduction," SAE Int. J. Commer. Veh. **2**, 183 (2009).

[35] R. McCallen, K. Salari, J. Ortega, P. Castellucci, D. Pointer, F. Browand, J. Ross, and B. Storms, "DOE project on heavy vehicle aerodynamic drag," Technical Report No. UCRL-TR-227076 (Lawrence Livermore National Laboratory (LLNL), Livermore, CA, 2007).

[36] B. Storms, D. Satran, J. Heineck, and S. Walker, "A study of Reynolds number effects and drag-reduction concepts on a generic tractor-trailer," AIAA Paper No. 2004-2251, 2004, p. 2251.

[37] K. R. Cooper and J. Leuschen, "Model and full-scale wind tunnel tests of second-generation aerodynamic fuel saving devices for tractor-trailers," Technical Report No. 2005-01-3512 (SAE Technical Paper, 2005).

[38] M. Lenngren and C. Håkansson, *CFD Analysis of Aerodynamic Trailer Devices for Drag Reduction* (Chalmers University of Technology, 2010).

[39] K. H. Lo and K. Kontis, "Flow characteristics over a tractor-trailer model with and without vane-type vortex generator installed," J. Wind Eng. Ind. Aerodyn. **159**, 110–122 (2016).

[40] K. H. Lo and K. Kontis, "Flow around an articulated lorry model," Exp. Therm. Fluid Sci. **82**, 58–74 (2017).

[41] L. Taubert and I. Wygnanski, "Preliminary experiments applying active flow control to a 1/24th scale model of a semi-trailer truck," *The Aerodynamics of Heavy Vehicles II: Trucks, Buses, and Trains* (Springer Berlin Heidelberg, 2009), pp. 105–113.

[42] J. Xie, C.-H. Liu, Z. Mo, Y. Huang, and W.-C. Mok, "Near-field dynamics and plume dispersion after an on-road truck: Implication to remote sensing," Sci. Total Environ. **748**, 141211 (2020).

[43] D. S. Gross and W. S. Sekscienski, "Some problems concerning wind tunnel testing of automotive vehicles," SAE Trans. **75**, 593–607 (1967).

[44] A. Sciacchitano and B. Wieneke, "PIV uncertainty propagation," Meas. Sci. Technol. **27**, 084006 (2016).

[45] M. Djeddou, A. Mehel, G. Fokoua, A. Tanière, and P. Chevrier, "On the application of statistical turbulence models to the simulation of airflow inside a car cabin," Phys. Fluids **35**, 025106 (2023).

[46] *Lectures in Mathematical Models of Turbulence*, edited by B. E. Launder and D. B. Spalding (Academic Press London, New York, 1972), pp. 7 and 169.

[47] V. Yakhot and S. A. Orszag, "Renormalization group analysis of turbulence. I. Basic theory," J. Sci. Comput. **1**, 3–51 (1986).

[48] T. Shih, "A new ke eddy viscosity model for high Reynolds number turbulent flows/. shih, ww liou, a. shabbir," Comput. Fluids **24**, 227 (1995).

[49] D. C. Wilcox *et al.*, *Turbulence Modeling for CFD* (DCW Industries, La Canada, CA, 1998), Vol. 2.

[50] F. R. Menter, "Two-equation eddy-viscosity turbulence models for engineering applications," AIAA J. **32**, 1598–1605 (1994).

[51] ANSYS Fluent, *Theory Guide 19.2* (ANSYS Inc., 2018).

[52] B. E. Launder, G. J. Reece, and W. Rodi, "Progress in the development of a Reynolds-stress turbulence closure," J. Fluid Mech. **68**, 537–566 (1975).

[53] C. G. Speziale, S. Sarkar, and T. B. Gatski, "Modelling the pressure–strain correlation of turbulence: An invariant dynamical systems approach," J. Fluid Mech. **227**, 245–272 (1991).

[54] K. Zore, B. Sasanapuri, G. Parkhi, and A. Varghese, "ANSYS mosaic polyhexcore mesh for high-lift aircraft configuration," in Proceedings of the 21st AeSI Annual CFD Symposium (2019).

[55] R. H. Croll, W. T. Gutierrez, B. Hassan, J. E. Suazo, and A. J. Riggins, "Experimental investigation of the ground transportation systems (GTS) project for heavy vehicle drag reduction," Technical Report No. 960204-3 (Sandia National Laboratory (SNL-NM), Albuquerque, NM, 1995).

[56] H. Choi, J. Lee, and H. Park, "Aerodynamics of heavy vehicles," Annu. Rev. Fluid Mech. **46**, 441–468 (2014).

[57] J. C. Hunt, A. A. Wray, and P. Moin, "Eddies, streams, and convergence zones in turbulent flows," in *Proceedings of the 1988 Summer Program* (Studying Turbulence using Numerical Simulation Databases, 1988).

[58] H. J. Lugt, "The dilemma of defining a vortex," in *Recent Developments in Theoretical and Experimental Fluid Mechanics* (Springer, 1979), pp. 309–321.

[59] J. Jeong and F. Hussain, "On the identification of a vortex," J. Fluid Mech. **285**, 69–94 (1995).

[60] S. K. Robinson, "Coherent motions in the turbulent boundary layer," Annu. Rev. Fluid Mech. **23**, 601–639 (1991).

[61] R. W. Metcalfe, A. Hussain, S. Menon, and M. Hayakawa, "Coherent structures in a turbulent mixing layer: A comparison between direct numerical simulations and experiments," in *Turbulent Shear Flows 5* (Springer, 1987), pp. 110–123.

[62] A. F. Hussain and M. Hayakawa, "Eduction of large-scale organized structures in a turbulent plane wake," J. Fluid Mech. **180**, 193–229 (1987).

[63] D. Bisset, R. Antonia, and L. Browne, "Spatial organization of large structures in the turbulent far wake of a cylinder," J. Fluid Mech. **218**, 439–461 (1990).

[64] M. S. Chong, A. E. Perry, and B. J. Cantwell, "A general classification of three-dimensional flow fields," Phys. Fluids A: Fluid Dyn. **2**, 765–777 (1990).